A Topological Study of a Surface Signaling Network and Possible Implications for Neural Dynamics

AUTHORS

Siddhartha Sen[1,2], Tomás J. Ryan[3,4,5], David Muldowney[2], Plamen S. Stamenov[2], and Maurizio Pezzoli[4]

AFFILIATIONS

[1] Centre for Research in Adaptive Nanostructures and Nanodevices, Trinity College Dublin, Ireland.
[2] School of Physics, Trinity College Dublin, Ireland.
[3] Florey Institute of Neuroscience and Mental Health, Melbourne Brain Centre, University of Melbourne, Victoria, Australia.
[4] Child & Brain Development Program, Canadian Institute for Advanced Research (CIFAR), Toronto, Ontario, Canada.
[5] School of Life Sciences, École Polytechnique Fédérale de Lausanne, Switzerland.

SUMMARY

Theoretical neuroscience is progressing strongly with novel representations of the brain, enhanced by the constant increase of computational power now available. New models suggest new ways to understand how complex brain events are emerging and explore the mechanisms of storing memory. However, there are major conceptual theoretical problems that remain unaddressed. Current theoretical methods are very capable reacting to experimental results and modeling both neural signaling and structure. Yet they still fall short to throw light on how the brain creates its own information code, or relate the variety of brain signals observed, or explain where and how memories are stored. We present here with topology as our main tool, a mathematical structure that demonstrates that circuit architecture and signal can correlate, while preserving information. This concept would imply a possible substrate for memory recording, that despite so far not been observed in biological organisms, has been already demonstrated on solid state physics and is consistent with conventional understandings of neurobiology.

INTRODUCTION

Experimental progress in neuroscience has been remarkable. New tools and methods of studying the brain have led to insights regarding neural activity and memory storage. The consensus is that sensory input signals carry information that processed by the brain, gives rise to our sensory experiences. By internal mechanisms the brain evaluates saliency and relevancy of the sensory experience, which might trigger that the event is then stored within the neural circuit as long-term memory. The process of memory creation has been studied in depth but where memories are actually stored is still under investigation. It is generally accepted though, that is through neuronal firing within the circuit that all these processes begin to take place. The most basic neural excitation, the action potential, is well described by the Hodgkin Huxley equations [Scott 2002]. Action potentials are described in terms of the inflows and outflows of ions controlled by protein channels present in neural membrane and their properties. From a neuron, there is one signal exit fiber, the axon. Action potentials enter the soma, the cell body of a neuron through its signal receiving dendrites. If the input signals cross a certain threshold value, a processed action potential exits the neuron via its axon. The signals are observed electrical voltage pulses and are assumed to satisfy Ohm's law of electromagnetism. Electric pulse currents flows are dissipative. They lose energy as they move. By their nature dissipative waves, are not capable of carrying information. In dissipative waves there is a causal cycle of energy injection and energy dissipation, in this case the energy injection comes from membrane ion inflows and outflows, that lead to a potential gradient while the dissipation comes from the ohmic current created by the potential gradient. This causal cycle propagates the signal. It is thus driven by the membrane properties and does not depend on how the signal was created. This means that the individual action potential pulses cannot carry information [Scott 2002] regarding the way they were generated. But we do know that action potentials are produced directly in response to excitatory inputs and we also do know that the information carried by action potentials evoked by our senses convey messages to the brain that allows us to see, taste, hear, and feel sensations. But the theoretical representation of action potentials as dissipative waves thus does not have this intuitive link between the signal and information. The current answer [Bialek 1991] on how is this conundrum resolved in the theoretical approach, is that information is postulated to be carried, not by individual pulse but by the rate at which the pulses are generated or by the unknown gaps between them. The way this is done is not known. If information is carried indirectly, then a proper theory would identify in what way sensory data is carried by the distribution or rate of production of action potentials.

A major area of interest in neuroscience that is how memories are created and how they are stored. There is compelling experimental evidence that a complex chain of biological processes take place within neurons during memory creation, such as long-term and short-term synaptic plasticity, but less is known about how memories (and the information within them) are stored. What is known is that memories are not stored in independent neurons or their synapses, but perhaps non locally in an unknown way, in the pathways between special group of neurons, in a structure called an engram [Ortega 2022]. There is experimental support for this picture [Liu 2012, Ryan 2015], but the lack of a theory for engrams is problematic. Ideally, a theory should explain how action potentials carry information, if not in the pulses themselves, then in their production rates or distributions in a way that is theoretically understood. The theory should then be able to explain how such information is stored to form memories. Each step should be testable. Currently there is no such explanation available.

A brain is an autonomous system, that creates its own information code and use it to store information and retrieve them easily. Signal production has two parts, input signals, carrying information and output signals that lead to sense perceptions, mode changes and actions. Current theoretical methods are reductionist. They do not link the brain's information code directly to action potentials, they do not suggest an autonomous way of describing brain input signals that clearly relate them to the inputs they receive, they do not have an autonomous method of generating signals and are not capable of dealing with global properties of the brain. Current observational neuroscience memory research on the other hand, reveals that global features of the brain are important not just for memory but for its functioning as a distributive global system.

Here we present theoretical approach that aims to take steps towards overcoming this gap. By means of a mathematical frame we create a system that describes a network capable of creating signals and

storing memory within the structure of the net. In this system, signal and structure are linked mathematically.

THE FRAMEWORK

We next present a mathematical object that attempts to describe an electroconductive, signaling surface network The approach shows how signal generation can be a global process involving transient topology changes to its subunits. The surface itself can be pictured as a two-dimensional cover of a complex converging and diverging network, with branchlike three-dimensional architecture. Our analysis of the surface uses the ideas of topological connectivity (Munkres 2014, Nash 1988).

Certain restrictions on the nature of the surface must be added for the sake of providing a proper network description. First, it must be orientable. This means that the surface has two sides. Second, the surface has to have topological connectivity properties. This means it contains a multitude of tubes joined together, in different regions, to form a connected surface without boundaries. The topological classifying theorem for surfaces (Munkres 2014), tells us that any surface without boundaries, no matter how complex, constructed as described, can always be rearranged to look like a sphere with *g* tubes attached or as a set of connected *g* donuts (tori) surfaces (Fig 1). The number of donuts or the number of surface tubes on a sphere is called the genus or genus number of the surface. It is fixed by the form of the algebraic equation that parametrizes the surface. Ours is a surface of high genus number. The surface of a sphere has a genus 0, the surface of a torus has a genus 1, our surface has then a genus *g* (Fig 1A).

We suppose our surface network is smooth. This allows us use ideas of surface calculus in our analysis (Bak 2010). Then, such a network can be described by using topological coordinates that are a set of special 2*g* closed loops ($a_1, a_2, \ldots a_g; b_1, b_2, \ldots b_g$).

A two-dimensional, orientable smooth surface of the kind described is called a Riemann Surface. (Appendix I).

The set of topological loop coordinates are geometrical objects that provide a representation of the connectivity features of the Riemann Surface. While the smoothness of a Riemann Surface of genus *g* $\sum_g$, is represented by a set of *g* smooth one-forms (Munkres 2014). One-forms are objects that can be integrated along one-dimensional loops or paths (Appendix II).

These two sets of mathematical objects that describe a Riemann Surface can be used to introduce a set of variables, which in turn can be used to define a natural algebraic function that represents the Riemann Surface. The algebraic variables are obtained by simply integrating the set of *g* smooth one-forms over the set of 2*g* loop coordinates of $\sum_g$ to produces a set of 2*g* numbers, or integrated over paths with a fixed starting point and a variable point *z* of the Riemann Surface to generate a set of *g* variable points. Smooth one-forms are called holomorphic differential one-forms (Appendix II A).

We write holomorphic or smooth one-forms as, $\omega_i(u)du$. Smoothness means that the functions that multiply du can be differentiated an arbitrary number of times with respect to the complex variable u. The *g* one-forms as well as the 2*g* loops topological coordinates, necessary to describe our surface-network, a Riemann Surface of genus *g*, can be constructed using the mathematical result that all Riemann Surfaces can be parameterized by polynomial algebraic equations in terms of two complex variables (Teleman 2003, Appendix I). In our case the relevant algebraic equation is called a real hyperelliptic equation. This equation parametrizes our surface network.

A real hyperelliptic equation for a genus *g* Riemann Surface is defined by,

$$y^2(u) = \prod_{i=1}^{2g+2} (u - a_i)$$
$$= P(u)$$

Where u, y are complex numbers but $a_i,\ i = 1, 2, \ldots (2g + 2)$ are either all real numbers or they occur as a pair of complex conjugate numbers. The way to construct our genus *g* Riemann $\sum_g$ from this equation is described (Appendix III).

To make our surface electroconductive we next introduce charges on $\sum_g$ as surface electrons. This step introduces a new topological feature to the surface, namely, a topological spin structure. This is because the electrons are spin half particles that have magnetic properties which allows them to form different topologically inequivalent patterns (Atiyah 1971, Mumford 1971).

Our surface network now has electroconductive properties as electrons carry charge, while at the mathematical level it has two layers of topology: one reflecting its topological connectivity, given by its non-zero genus ($g > 0$) and the other from the presence of surface electrons, that gives the system a spin structure. These two topological properties have associated with them topological numbers. Thus, the topologically distinct arrangements of linked surface electron spins carry a topological charge number *W*, which we will discuss later, while the connectivity topology of the surface is given by its genus *g*. Since the surface is now charged, all local topological surface distortions will generate local voltage variations (Appendix IV).

Thus, to summarize, we have described an electroconductive surface network, a special Riemann Surface of genus *g* ($\sum_g$) with spin structure that has topological properties that are given by two numbers (*g*, *W*), which is parametrized by a real hyperelliptic equation.

LOCAL TOPOLOGICAL DISTORTIONS

We now make our $\sum_g$ into a dynamical system by introducing a dynamical law that defines the nature of allowed input signals to the system and then determines the system's response to them. Our dynamical law states that both the input signals and responses to them must respect the mathematical properties of the Riemann Surface network. Keeping this requirement in mind we define input signals, local deformations, in terms of objects that are well defined on a Riemann Surface (Appendix II A). But before this can be done, we will have to introduce some mathematical ideas and explain the geometric nature of the input signal, a pinch deformation, in terms of Riemann Surface variables. Later we will show how the dynamical law also determines the nature of responses to pinch deformations.

A pinch deformation as an input signal, is a local geometric distortion of the surface that reduces the circumference of a loop a_i at a point to zero (Fig 2A). It is the universal input signal of the network. Such a deformation also changes the topology of the subunit in which it occurs and initiates charge movement (Appendix IV).

To describe the dynamics of these geometrical deformations to the Riemann Surface we need to introduce an appropriate algebraic function. Then, we show, a geometric pinch can be described in algebraic terms. To do this we use the natural variables of the Riemann Surface. Since a pinch deformation corresponds to reducing a circumference of a a_i loop at a point, an algebraic description of this process can be obtained by taking the loop integral of a one-form along the loop that is getting deformed. As the loop shrinks to zero, we now have an algebraic representation with deformation parameters of the process in terms of the natural variables of the Riemann Surface (Appendix II B).

Such a pinch deformation reduces the circumference of a single a_i loop at a point to zero, thus transiently reducing the genus of $\sum_g$ from *g* to *g* - 1.

NODE EVENT

We explained how a natural set of deformation parameters that identify the nature of pinch deformation input signal can be introduced (Appendix II B). A set of simultaneous pinch deformations of a subunit of $\sum_g$ of genus $k < g$ ($\sum_k$), that reduce these topological numbers of the subunit to zero, creates a transient topological sphere (Fig 2B). We define this process as a node event.

We next explain how the response of the surface network to such pinch inputs can be obtained from the dynamical law. In this case, the dynamical law can be viewed as a compatibility condition. To proceed we next use the fact that the algebraic function used to describe the $\sum_g$ is valid only if the function satisfies a nonlinear constraint (Mumford 1984). Under pinch deformations that we consider, this nonlinear constraint becomes a set of nonlinear differential equations, known as the nonlinear Schrödinger differential equations (Kalla 2012). Thus, the dynamical law requires that the response functions to pinch deformations must be solutions of these equations for the responses to be compatible with the mathematical Riemann Surface structure.

We now have a dynamic input-output set up for our surface network, where local pinch deformations are input signals that produce output pulses that are solutions of a set of nonlinear Schrödinger differential equations. This scheme of signal generation is established, not on the basis of observational inputs, but from a mathematical analysis of compatibility that exploits the topological features of the special electroconductive surface network.

We observe that as pinch deformations reduce the circumferences of a set of *k* a_i loops to zero, they transiently reduce the genus of $\sum_k$ from its genus value *k* to zero which also reduces its topological spin structure charge *W*, to zero. Since our surface is charged, these distortions will generate local voltage variation pulse signals (Appendix IV B and VII) that carries away the topological numbers of the network as well as the pinch deformation details with them.

We have described the properties of $\sum_g$ that we use for our surface network and described how it produces signals. We have also stressed that the dynamics of the network is determined by a dynamical law that requires that both input and output signals in the network respect the underlying mathematical Riemann Surface structure of the network under distortions or deformations. Our next step is to introduce the algebraic function used to describe our special surface network, the Riemann Theta (θ) Function, and the Fey Trisecant Identity it must satisfy if it is to describe a Riemann Surface (Sen 1988). With these technical details in place, we then can proceed to study the node events.

RIEMANN THETA FUNCTION

We have already described how $\sum_g$ is defined in terms of 2*g* topological coordinate loops (a_i, b_i), $i = 1, 2, \cdots g$; and *g* one-forms $\omega_i(u)du$. From them we first generate a set of algebraic variables (n_i, z_i, Ω_{ij}) that capture geometric and smoothness features of the Riemann Surface and then use them to define the Riemann Theta Function. These variables were already described in an intuitive way, now we give the formal definitions and explain that they have geometric and topological meaning.

We start by normalizing one-forms so that an integral once round a_i loop is, either plus or minus,

$$\int_{a_i} \omega_i(u)\, du = \pm 1$$

The result represents a topological winding number associated with the loop a_i. The two signs correspond to the two possible ways winding can happen; clockwise or anticlockwise. Thus, associated with a loop a_i one can associate a winding n_i, which can take any possible integer value.

Next, for any given point z of $\sum_g$ it is possible to generate *g* complex numbers by

$$z_i = \int_{z_0}^{z} \omega_i(u)\, du$$

with $i = 1, 2, \cdots g$, where z_0 is an arbitrary fixed point on $\sum_g$. Thus, a single variable point on the Riemann surface generates a set of *g* variable points that come from the presence of the *g* smooth one-forms of the Riemann Surface. This is a natural way of feeding in smoothness in an algebraic

way. Next, a complex matrix can be constructed by integrating one-forms, but this time over the b_i loops

$$\Omega_{ij} = \int_{b_i} \omega_j(u)\, du$$

with $i, j = 1, 2, \cdots g$. This matrix has been proved to be symmetric and its imaginary part positive (Mumford 1984). It describes the complex connectivity of the Riemann surface.

Finally, an additional set of variables (α_i, β_i) that can only take the values 0 or 1/2 can be introduced. These discrete variables are called characteristics and represent the spin structure of $\sum_g$ in an algebraic way in the Riemann Theta Function. The characteristics allow that fractional winding numbers when one-forms that are integrated around the a_i, b_i loops, are possible. (Atiyah 1971, Mumford 1971).

These characteristics can also be used to define topological number *W*.

$$W = 4 \sum_{i=1}^{g} \alpha_i \beta_i$$

With all variables required defined, we can now define the theta function with characteristics (Mumford 1984):

$$\theta_{[\alpha_i, \beta_i]}(\Omega, z_i) = \sum_{n_1, \cdots n_g = -\infty}^{+\infty} e^{\sum_{a,b} \pi i (n_a + \alpha_a) \Omega_{ab} (n_b + \alpha_b) + 2\pi i (z_a + \beta_a)(n_b + \alpha_b) \delta_{a,b}}$$

where $\delta_{a,b}$ is the Kronecker delta function.

The Riemann Theta Function depends on *g* complex numbers z_i

$$z_i = \int_{z_0}^{z} \omega_i$$

generated from two points (z_0, z) on $\sum_g$. Thus, the Theta Function is defined on a *g* dimensional space of complex numbers and has periodicity properties, inherited from the periodicity of the integrals of ω over the closed loops (a_i, b_i) of $\sum_g$. This complex space with the periodicity features factored out is the *g* dimensional space called the Jacobian, $J(\sum_g)$ (Mumford 1984). Points on $\sum_g$ on the other hand, are described by just a single complex variable. To understand how the Theta Function, defined on a space of *g* complex dimensions can represent $\sum_g$, a function of just one complex variable, we make use of the Jacobi Inversion Theorem (Guardia 2002) which is stated (Appendix V). The basic idea is that for *g* points on $J(\sum_g)$ there are *g* related points on $\sum_g$.

LOCAL DISTORTION WITHIN THE THETA FUNCTION

We now define local pinch deformations. In the pinch limit, the radius of a tube loop at a point on a surface is reduced to zero thus moving this point to the center point of the tube, which is a real number. This geometric pinch deformation process can be described in terms of an integral of one-forms along the tube loop. The set of one-forms close to the center point of the tube can be expanded as a Taylor expansion about the center point so that, intuitively, the distortion parameters correspond to the Taylor expansion's coefficients. Since there are *g* one-forms at a point on the surface, each distortion term will have *g* distortion parameters. To get a variety of response solutions it turns out to be necessary to expand the one-forms keeping only the first and third derivative terms (Arbarello 2002). Thus, the variables of the Theta Function collapse to a pair of real numbers that can be interpreted as (*x*, *t*) that are multiplied by factors $W_i, V_i, \quad i = 1, 2, \cdots g$ that represent the nature of the

pinch deformation (Appendix II B). Since under a pinch deformation the circumference of a tube at the pinch point goes to zero, and all *g* complex variables of $J(\sum_g)$ collapse to multiples of a single point of $\sum_g$ where the multiplying factors are the distortion input signal specific parameters. Thus, in the pinch limit the Riemann Theta Function now becomes a function on $\sum_g$ .We make these remarks clear by the following sketch where the technical details are omitted.

A pinch deformation at a point z on $\sum_g$ has an effect on the *g* variables z_i of the theta function. These variables are related by the equation

$$z_i = \int_p^z \omega_i(w)\, dw$$

with z and p as points on $\sum_g$, the latter being the fixed. Consider a circular arc path joining both points (Fig 2A). In the pinch limit, z approaches to p, i.e., $z \to p$ as the radius of the circle with center $z = z_0$ inside the tube, so that the arc length connecting both points, also becomes very small. Thus, we have

$$z_i \to \int_p^z \omega_i(w)\, dw$$

$$\to (z - p)\omega_i(z_0)$$

when z is close to p. As both of these points are close to the center of the tube, $z = 0$ we approximated $\omega_i(w)$ by its value at the center of the tube, namely by $\omega_i(z_0)$. With this done the *g* points of the theta function become

$$z_i \approx \omega_i(z_0)z$$

Thus, in the pinch limit all the variables of the Theta Function are proportional to the point z which is a point on $\sum_g$ close to the center of the tube. We have set $p = 0$. The proportionality factor $\omega_i(z_0)$, defines the nature of the pinch deformation at point z. This sketch is only illustrative. The proper technical set up is given elsewhere (Appendix II B). We conclude this section by making two remarks.

$\sum_g$ and the algebraic Riemann Theta Function can be constructed from a hyperelliptic equation but with spin structure information about $\sum_g$ added in, that is compatible with the hyperelliptic equation (Kallel 2010, Krazer 1903).

The hyperelliptic equation has important features. It allows the maximum possible spin structures on its associated Riemann Surface (Krazer 1903). It allows the maximum number of subunits connected Riemann Surface (Harnack 1876). This means it permits a large of specialized functional subunits of the network to exist, and it can generate a vast number of diverse non-linear excitations by pinch deformations on its subunits (Arbarello 2002, Kalla 2012).

RESULTS

We sketched some essential features of pinch deformations. We drew attention to the transient topological changes they initiate and the fact that the response signals generated by such pinch deformations can be shown to carry with them topological information as well as geometric pinch deformation information. With the mathematical representation fully in place we explore once more the node event. Pinching distortions have three effects: they increase local voltage values (since the surface is charged), they reduced the original genus *g*, and if enough pinching deformations are applied reduce the genus *g* of a system and its spin structure topology number *W* to zero value, and by these topological global processes produce one-dimensional signals.

The exact nature of response of the surface to such pinch deformations can be found by using the dynamical law for the network. The law states that since the Riemann Theta Function describes a

Riemann Surface $\sum_g$ only if it satisfies the non-linear Fay Trisecant Identity (Arbarello 2002, Sen 1988), (Appendix VI), all responses to deformations must satisfy the pinch deformed form of the identity, which in our case, gives the result that responses to pinch deformations are Theta Function solutions of a set of non-linear Schrödinger differential equations, where the variables of the Theta Function are distorted by the pinch deformation. This result applies to any subunit $\sum_k$ from $\sum_g$ ($k < g$) that is pinched. Thus, responses to pinch deformations in a subunit, produce responses that are Riemann Theta Functions with their variables distorted by the pinch deformations, which travel to other subunits of the network. In particular the response of a subunit of genus *k*, to *k* pinch deformations that reduces its genus to zero, are a train of *k* one-dimensional solitons, each of which carries the spin structure topological charge *W* as well as geometric pinch deformation information.

There is a variety of soliton solutions of the non-linear Schrödinger equation. Here we look at bright-soliton and dark-soliton solutions (Fig 3). They behave as propagating one dimensional pulse excitations through the surface of $\sum_g$. Non-propagating local transient solutions of the non-linear Schrödinger equation are also possible.

The one dimensionality of the solution comes from the fact that a pinch deformation forces surface points to the center of the tube pinched (Fig 2). The solutions do not describe the motion of the pinch point, but have a voltage profile determined by the nature of the local distortion and the global properties of the $\sum_k$ that participates to generate it. The idea is that a subunit $\sum_k$ generates a Riemann Theta Function signal that then propagates to other subunits $\sum_k$ by the interconnected network ($\sum_g$). Such a scheme is possible since a Riemann Surface represented by a hyperelliptic equation has a modular structure (Harnack 1876).

ANALYTIC EXPRESSION FOR MULTI-SOLITON AS VOLTAGE PULSES

The expression of multi-soliton pulses solutions (Mumford 1984), (Appendix VI and VII), can be numerically evaluated (Fig 3). An example (Kalla 2012) of such solution found is

$$\psi_j(x,t) = A_j \frac{\theta\left(\vec{Z} - \vec{d} + \vec{r}(j)\right)}{\theta\left(\vec{Z} - \vec{d}\right)} e^{-i\left(E_j x - F_j t\right)}$$

where

$$r(j) = \int_{a_{(k+1)}}^{a_j} \omega_j(z)\, dz$$

$$\vec{Z} = i\vec{V}_{a_{k+1}} x + i\overrightarrow{W}_{a_{k+1}} t$$

$$K_1(a,b) = \frac{1}{2}\frac{\Delta_a \theta[\delta](0)}{D_a \theta[\delta](0)} + D_a \ln\theta\,[\delta]\left(\int_a^b\right)$$

$$K_2(a,b) = -\Delta_a \ln\theta\left(\int_a^b\right) - D - a\ln\left(\theta\left(\int_a^b\right)\theta(0)\right) - \left(D_a \ln\theta\left(\int_a^b\right) - K_1(a,b)\right)^2$$

$$E_j = K_1\left(a_{k+1}, a_j\right)$$

$$F_j = K_2\left(a_{k+1}, a_j\right) - 2\sum_{i=1}^{k} q_1(a_{k+1}, a_i)$$

$$q_1(a, b) = D_a D_b \ln\theta\,[\delta]\left(\int_a^b\right)$$

$$q_2(a, b) = \frac{D_a\theta[\delta](0)D_b\theta[\delta](0)}{\theta[\delta]\left(\int_a^b\right)^2}$$

and $\vec{d}, A_j$ are constants. Each pulse soliton contains the same pinch deformation parameters through the variable $\vec{Z}$ (Kalla 2012). Solutions without oscillation factors have also been found (Previato 1985).

It should be noted that *k* pinches are involved in the solution $\psi_j(x,t)$. Thus, a large multi-soliton response is generated by contributions from a large number of pinch deformations.

Soliton solutions can be physically interpreted as voltage variations (Appendix IV B).

Numerical evaluations of multi-soliton solutions belonging to two different classes, bright and dark solitons are here determined. We consider four examples.

We illustrate the approach by numerically evaluating ψ_j^2 for four multi-solitons. Here we find first the dark solution for *k* = 3 and *k* = 2, and then invert them to obtain the bright soliton solutions (Fig 3). The soliton nature of both solutions is shown numerically.

In the numerical evaluations of the three and two pulses multi-soliton for dark and bright solutions are considered. It is found that not all input signal parameters lead to excitations. The solution's pinch deformation parameters fix the rate at which the soliton pulses appear, as well as the gaps between them through the parameters $\vec{Z}$ and $\vec{r_j}$ of the solutions where the parameters $T_{j,\beta}$ fixes the shape of those pulses.

We write

$$V = (a_k, b_k) = a_k + ib_k$$

$$W = (c, d) = c + id$$

$$i = +\sqrt{-1}, k$$

$$(V_k, W_k) = (a_k, b_k, c_k, d_k)$$

$$k = 1, 2, 3$$

The pinching loops for the *k* = 3, dark solutions are real points $(a_1 = -3.999, a_2 = -3.95, a_3 = -3.92, a_4 = -3.91)$, they are zeros of the hyperelliptic equation. The Riemann Surface is constructed using this information and choosing branch point locations in the complex plane located to be: (-4, -3, -2, -2 + ϵ, 0, 0, + ϵ, 2, 2 + ϵ), with $\epsilon = 10^{-10}$. The input data is displayed (Table 1).

Table 1

Pinch distortion	Code	Network	T or E
Pinch distortion (1)	(0, -2.5873, 0, 11.5975)	(1, 1, 1)	T
Pinch distortion (2)	(0, -309581, 0, 14.706)	(1, 1, 1)	T
Pinch distortion (3)	(0, -3.2384, 0, 15.6638)	(1, 1, 1)	T

For the k = 2 case the branch points are (-2, -1, 0 + ϵ, 2 + ϵ), The pinching loops are $(a_1 = -1.9, a_2 = -1.11, a_3 = -1.8)$. Input data displayed (Table 2).

Table 2

Pinch distortion	Code	Network	T or E
Pinch distortion (1)	(0, -1.9142, 0, 2.5916)	(1, 1)	T
Pinch distortion (2)	(0, -2.2790, 0, 3.6734)	(1, 1)	T

Solutions of the non-linear Schrödinger (NLS) equation represent responses to local pinch deformations of the Riemann Surface network studied. The equation has a non-linear term of the form

$$\sum_{i=1}^{k} s_i \psi_i(x,t)^2 \psi_j(x,t), \qquad j = 1,2 \cdot\cdot k$$

where $s_i = \pm 1$, for a soliton $\psi_j(x,t)$. Different choices for the sign factor s_i lead to different types of solutions. For dark solutions $s_i = +1$ for all k values, while for bright solutions $s_i = -1$ for all k values. Other sign selections produce voltage pulse excitations of different shapes and are topologically distinct.

The numerical solution fixed the index k of the solutions displayed to k = 2 and k = 3 to numerically determine two and three dark soliton solutions. The propagation speed of the solitons and their amplitudes found numerically can be adjusted by a suitable choice of scale parameters (Appendix IV B). In the case of k = 2 there are eight, and for k = 3 twelve distortion parameters. These parameters are assembled together by characteristics α_i that identify the section of the network responsible for the local distortion (i.e., excitation). All characteristics are set to be equal to 1/2, this means that in the soliton limit all network paths of the unit producing the signal are used. We note the vector $\vec{Z}$ fixes the rate at which the spikes pulses arrive. The solutions show that gaps between the soliton pulses and their rate of production carry information as they are sensitive to the pinch distortion parameter values used to generate them. The gaps depend on the form of the period matrix in the pinch limit.

The multi-soliton pulses have an information carrying substructure that originates from input distortion signal parameters at multiple pinch locations of the surface of the network. This substructure is carried directly by the solutions and also indirectly in the appropriate connectivity matrix elements Ω_{ij} of the network responsible for such signal. The multi-soliton pulses then can transport and carry the pinch distortion details.

DISCUSSION

Using topology as an approach, we introduce a special surface network that can generate a wide variety of one-dimensional voltage pulse signals, that carry transient structural information regarding local inputs, here described as topology changing local pinch deformations. The mathematical constrains to achieve such a system requires to describe the network as a special Reimann Surface that can be parametrized by the algebraic hyperelliptic equation and it must have surface electrons. The dynamical law for this case requires that all activities of the network must conform to the mathematical structure of the surface introduced. Thus, both input signals as well as the responses

they produce are required to satisfy the mathematical properties of our special Riemann Surface. Local deformations of the network incorporate local input signals within the restrictions of the proposed lattice. To study the dynamical behavior under deformations we introduced the Riemann Theta Function, but for this description to be valid the Theta Function has to satisfy the Trisecant Identity (Fay 1973). Under the local deformations introduced, the Identity becomes a set of nonlinear Schrödinger (NSL) equations.

We pointed out that pinch deformations, which have signal specific geometric distortion parameters, also change the two topological structures present in the network: one coming from its connectivity and the other from the spin of the surface electrons. Then, the signals generated carry with them both, the geometric and the topological information respectively. Is under that scope that the signal carries transient structural information. Transient, because it is a traveling signal, and structural because the signal carries within, the parameters of the structure that produced it.

It then becomes relevant to consider if the framework here presented can overlap with the current view of neural circuits dynamics observed in biology. At first, a strict topological point of view could argue that the cellular theory of the brain, tells us that the circuit is formed by an intricated net of connecting topological spheres, or neurons and glial cells. But this physical connectivity alone does not sustain the functionality of the network, in the sense that a living brain and a dead brain would have the same anatomical layout, but not the same functionality. Its prime task is signal transmission, and for that the neural circuit first it must be polarized by keeping a measurable and sustained voltage difference between the extracellular and the intracellular of neurons. It is of such relevance, that it is maintained at metabolic expense. If we focused then in that electrochemical cloud, generated by different biochemical pumps, and sustained by the capacitance voltage present on the neural membranes, one could observe a connected layer surrounding tube structures, made by the edge of higher concentration of Na^{+} and Ca^{2+}, kept in position around neural membrane by their respective electrochemical gradients. Synaptic connections could still arguably be a disconnection, but if observed from within the intracellular space for both ends (pre and post synaptic), the Na+/Ca2+ higher concentration layer remains outside of the membrane, as long as it is properly polarized (resting membrane potential), providing some base that it could be understood as a sort of virtual connection of the tube network. Gap junctions would also help providing a picture of a surface continuum. Ionotropic excitatory synaptic transmission then would become topologically fixed events, a localized “collapse” of the polarized tube-space driven by local ionic currents, behaving as the described pinch deformation. Recent investigations (Cornejo 2022) using voltage sensors have shown that dendritic spines compartmentalize voltage changes, and for voltage changes to be sensed by the complete neuron, it must incorporate a full section of a dendritic branch and not just spines, presenting a punctual depolarization in the branch, collapsing the continuity of the proposed polarized virtual tube. In this framework, neurons (as nodes) would behave as coincidental excitation detectors, imbibing the generated signals with structural information.

Solitons $\psi(x,t)$, as traveling non dissipative signals, are electromechanical pulses (Appendix IV B) that would be observed in the electric charge, as well as a “mechanical” pulse in the lattice of the theoretical surface (Fig 3). A similar phenomenon has been observed on axons when firing action potentials (El Hady 2015). In addition, the N-soliton dark solution (Previato 1985) is able to fit electrophysiological data of a firing neuron triggered by presynaptic stimulation (Fig 5, Appendix VIII).

Interestingly the structure here proposed predicts that such traveling electric signals, if strong or repetitive enough, and because they are one-dimensional current pulses traveling through the center of an electrocharged tube, would generate a helical non-transient structure on the surface itself, preserved by electron spin (Appendix IX). Because these helical structures are generated by a signal that is defined by parameters present in the Theta Function, they themselves would also be defined by the same parameters (Appendix VII and IX). An engraving event into a sensitive lattice, which is generated and corresponds to the same signal that was transmitted, is remarkably similar with the original concept proposed as a “mnemonic trace” or engram, in memory theory (Semon 1904).

It has been shown that memory can persist in the structure of the neural circuit despite the loss of recall in cases of amnesia (Guskjolen 2018, Ryan 2015). This scheme here presented offers a new possibility for memory traces, one that incorporates topological location, connectivity, and signals,

while offering a unifying consistency. The hypothetically structural transient information (i.e.: the topological parameters carried by the soliton, a traveling pulse) could then be recorded in a non-transient structure within the network itself, and by this we mean a magnetic, helical structure on the surface through where the signal passed, made stable and permanent, by the interaction of spins present in the surface electrons that were affected and aligned by the original passing signal (Appendix IX). There is as yet no evidence of such magnetic helical structures in biology, but the magnetic field of action potentials along the axonal tube has been measured and used to accurately reconstruct the shape of action potentials (Barry 2016), and the proposed structure has been observed to form in solid state physics (Uchida 2006). A speculation for a cellular rigid structure that can contain a dense array of molecules arranged in tubular rings on which then electrons (spinors) are organized, through which current is passed orthogonally, can find some correspondence with protein rich structures through which action potential travels, such as the axon initial segment (Hamdan 2020, Leterrier 2018) or the nodes of Ranvier (D'Este 2017, Rasband 2016).

Hypothetically then, if these conditions were to be met, it could be possible that synaptically elicited action potentials would carry architectural information of the circuit and synapse locations that produced it as a set of parametrical values. As well, an action potential as an electrical pulse could in turn engrave the circuit (if the described spin structure is present) with a trace that possesses the same parametrical values, then preserving such information.

The current work presents a new concept for a signaling network, one in which signal and structure are demonstrated to correlate mathematically. The system offers a framework where structure, signaling, and memory traces are possible, providing a feasible structure for a self-consistent network. This in itself proposes a novel, more holistic point of view which could provide a new light into aspects of biological neural dynamics.

APPENDIX

I. Riemann Surface

A mathematical result tells us (Teleman 2003) that all Riemann Surfaces can be viewed as geometrical representations of polynomial equations of two complex variables, $P(z,w) = 0$, where,

$$P(z,w) = a_0(z) + \cdots a_i(z)w^i + \cdots a_m(z)w^m = 0$$

and the coefficients $a_i(z)$ are polynomial functions of z. The degree *n* of the polynomial, which means the highest power of $n = l + k$ of terms $z^k w^l$ present in $P(z,w)$ fixes the genus *g* of the surface to be

$$g = \frac{(n-1)(n-2)}{2} - N_s$$

where N_s is the number of singular points of the polynomial equation, that is points where;

$$\frac{\partial P(z,w)}{\partial z} = 0$$

Thus, a Riemann Surface is a geometrical representation of a polynomial equation of two complex variables with its genus fixed by the nature of the polynomial. This representation defines the notion of smoothness of the surface. The smoothness of a surface means that the defining polynomial equation can be differentiated an arbitrary number of times. The applying of the classifying surfaces theorem (Munkres 2014), tells us that the Riemann surface of genus *g* can be represented as a connected surface of *g* donuts (tori). Using this representation, the connectivity properties of $\sum_g$ can be described by topological coordinates that are a set of 2*g* closed loops $(a_1, a_2 \cdots a_g;\ b_1, b_2 \cdots b_g)$ (Fig 1B). A particular choice of loops is called marking. The loops chosen are orthogonal which means that two loops from set A $(a_1, a_2, \cdots a_g)$ or set B $(b_1, b_2, \cdots b_g)$ in general do not intersect but a loop a_j from A intersects with loop b_j form B once.

We write these geometric properties as

$$(a_i, a_j) = (b_i, b_j) = 0$$

$$(a_i, b_j) = \delta_{i,j}$$

where $\delta_{i,j} = 1$, when $i = j$ and is zero when $i \neq j$.

There is an additional set of 2*g* discrete parameters called characteristics (Mumford 1984), that can only take the values 0 or ½, and are associated with each loop of the sets A, B. The characteristics describe the spin structure of a Riemann surface.

II.A One-forms

The smoothness properties of a Riemann Surface $\sum_g$, with surface points represented by a complex number u, are represented by a set of *g* linearly independent holomorphic differential one-forms $\omega_i(u)du$, $i = 1, 2, \cdots g$ on $\sum_g$ (Mumford 1984).

It has been shown that on a Riemann Surface exactly *g* linearly independent holomorphic one-forms exist. This means that any holomorphic on $\sum_g$ can be written as a linear combination of them with constant coefficients.

A one-form is an object that can be integrated.

Thus, if we write an integral

$$\int f(u)du$$

then,

$$f(u)du$$

is a one-form.

II.B Pinched one-forms

We define mathematically a local distortion or pinch deformation. We use the one-forms $\omega_j(u)$ on a Riemann Surface of genus *g* that represents a real hyperelliptic equation. We showed that they are given by

$$\omega_j(u) = \frac{z^{j-1}du}{\sqrt{P(u)}}$$

where

$$P(u) = \prod_{i=1}^{(2g+2)} (u - a_i)$$

Thus, these one-forms depend on the $(2g + 2)$ roots of $P(u)$. We also saw that the a_i cycles of $\sum_g$ have circumferences related to the difference between adjacent roots, $(a_{i+1} - a_i)$ of $P(z)$. Hence a pinch corresponds to two roots of the hyperelliptic equation approaching one another, since when this happens the circumference of the corresponding loop $a_i \to 0$. The pinch point is taken to be inside the interval. There are *g* cycles that can be pinched.

There are *g* functions $\omega_j(u)du$ whose variables can be deformed differently at a given surface point *p*. This point *p* has two coordinates p_a, $a = 1, 2$ so that we can write a local distortion as

$$\omega_j\left(p_a + \delta_{a,j}(p)\right)$$

We then can write

$$p = F\left(z_1, .. z_g\right) = F(\vec{z})$$

as a function of *g* variables of $J\left(\sum_g\right)$. This is an inverse of the map $p \to \left(z_1, .. z_g\right)$. This function is not known. Putting all these pieces together we can write the pinch deformed one-form $\omega_j(p)$, near the pinch point *p* as,

$$\omega_j(p) = \left(V_{a,j}(p) + W_{a,j}(p)k_a(p) + U_{a,j}\frac{k_a(p)^2}{2} + ..\right)dk_a(p)$$

$$D_a F(\vec{z}) = \sum_{j=1}^{g} \partial z_j F(\vec{z})\, V_{a,j}$$

$$\Delta_a F(\vec{z}) = \sum_{j=1}^{g} \partial z_j F(\vec{z})\, W_{a,j}$$

The set of points $j = 1, 2, .. g$ represent pinch locations while $k_a(p),\ a = 1, 2$ can be identified with a point on $\sum_g$. While the functions $V_{a,j}(p), W_{a,j}(p)$ are the signal specific pinch distortion functions on $\sum_g$ that represent the distortion of the signal generated.

This procedure of deformation described when imposed on the nonlinear Fay Trisecant Identity, turn the identity into a set of nonlinear differential equations known as the nonlinear Schrödinger equation (NLS). The Riemann Theta Function with pinch deformed variables must now be solutions of the NLS in order for it to continue to represent the Riemann Surface. These are soliton solutions (Kalla 2012).

III. The hyperelliptic equation $P(u)$ description of a Riemann Surface $\sum_g$

The hyperelliptic equation is given by,

$$y^2 = P(u)$$

Which can be written as,

$$y = \pm\sqrt{P(u)}$$

Near a zero point x_a of $P(u)$ the function becomes

$$P(u) = (u - x_a)K$$

when all the zeros are distinct. Setting

$$w = (u - x_a)$$

we have

$$P(w) = wK$$

Thus, a circle round $w = 0$ changes the sign of y due to the fact that a square root function changes sign under a full circular rotation. Thus, such a function It is not well defined. It's value at a point depends on its history. This problem is overcome by introducing a branch cut, a line, that starts at the point $w = 0$, and the rule that when circling round the point $w = 0$ this line cannot be crossed but the variable moves on to another copy of the complex plane. By this means the function y can be made a well-defined function of the variable z near all its zeros. Thus, the zeros of $P(u)$ determine (Belokolos 1994) the branch point locations of y that defines the cuts necessary to make $y(u)$ well defined. These cuts define the topological coordinates of the Riemann Surface associated with the hyperelliptic equation, namely its homology cycles, $a_i, b_i,\ i = 1,2,..g$ as suitable circuits round the branch points. In particular the a_i cycles, that represent loops round the circumference of tubes of $\sum_g$, are constructed as circuits round a pair of neighboring zeros of $P(u)$ linked together by a branch cut. We next write down the rule for constructing *g* smooth one-forms from $P(u)$. We have

$$\omega_i(u)du = \frac{u^{i-1}du}{\sqrt{P(u)}}\ ,\quad i = 1,2,..g$$

Now the complex variable u represents a point on the Riemann Surface of genus *g* constructed. We will replace u by z to represent such points. Thus, we have sketched how the topological cycles (a_i, b_i) and the smooth one-forms ω_i that define a Riemann Surface can be constructed starting from a hyperelliptic equation.

IV.A Voltage variations on $\sum_g$; Local distortions

The topological tube or handle has electrical and geometrical properties. As charged per definition, we can consider our surface a dynamic dipole layer. The voltage difference of the dipole is then defined as V_0.

We want to estimate the equilibrium value between strips of the surface separated by the diameter *r* of the surface tube. The calculation uses the electrical properties and the dynamic laws of quantum electrodynamics. It has been shown (Feinberg 1970) using quantum electrodynamics that there is an attractive Casimir-Poldar potential $V_{CP}(r)$, between charged dynamic dipoles layers separated by a distance *r*. The attractive potential is balanced by the elastic properties of the tube and the space contained by it.

We have then

$$V_{CP}(r) = -\frac{V_0}{r^7}$$

which is an attractive potential energy between dynamic neutral particles. It can be understood as a resting potential. Variations of *r*, are then result in voltage changes that reflect changes in the resting potential value.

IV.B Voltage variations on $\sum_g$; Soliton solutions

All the variables, functions and equations used are dimensionless. This allows flexibility on the nature of the system described. Then, multi-soliton solutions may be interpreted as voltage pulses. Consider the following non-linear Schrödinger equation with dimensional parameters,

$$i\frac{\partial}{\partial t}\psi = -D\nabla^2\psi + g\psi^2\psi$$

where t is time units, x is in length units, D is a dimensional diffusion constant, ψ is in volts and g is a dimensional constant which is a measure of non-linearity. We can rewrite this equation using dimensionless variables, we have

$$t \to \tau = \frac{t}{t_0}$$

$$x \to \frac{x}{x_0}$$

$$D \to D_0 = \frac{x_0^2 D}{t_0}$$

$$g \to g_0 = \frac{g V_0^2}{t_0}$$

Then once units for t_0, x_0, V_0 have been chosen, the response solutions generated will represent one-dimensional non-dissipative voltage pulses, and the pinch deformations can be understood as input signals as they induce local voltage changes.

V. The Jacobi Inversion Theorem

The equivalence of $\sum_g$ and $J(\sum_g)$ is at the level of certain abelian groups called divisors. For $\sum_g$ a divisor *D* is the formal sum of selected points on $\sum_g$ multiplied by integers. These groups establish a relationship between the number of zeros on $\sum_g$ to the corresponding number of zeros of the Riemann Theta Function on $J(\sum_g)$. We have

$$D = \sum_p n_p p$$

The degree of a divisor is defined as

$$degD = \sum_p n_p p$$

For a meromorphic function $f : \sum_g \to C$, a natural notion of a divisor (f) can be introduced. We write

$$(f) = \sum_p \left(ord_p(f)\right)_p$$

This is an enrichment of $\sum_g$ as further structures namely special types of functions are introduced on it. A meromorphic function has simple zeros and poles. The order at a simple pole is minus one, while at simple zero it is plus one. A general result is that the sum of the orders of zeros and poles of a meromorphic function on $\sum_g$ is zero. This translates to the statement that $deg(f) = 0$. We next introduce the Abel-Jacobi map, that maps point p on $\sum_g$ to points on $J(\sum_g)$. We must remember that a point in $J(\sum_g)$ is defined by *g* complex numbers. We have,

$$\mu: \Sigma_g \to J(\Sigma_g)$$

$$\mu = \left(\int_{p_0}^{p} w_i \, , i = 1, 2, \cdots g\right)$$

The point p_0 is a fixed reference point on $\sum_g$ with respect to which other points are linked by a path. It is possible to show that the linking path chosen does not matter. The map is then well defined.

This map extends to divisors. For point p in $\sum_g$ we have,

$$\mu\left(\sum_p n_p p\right) = \sum_p \mu(p)$$

We can now state the Jacobi Inversion Theorem: For every point in $J(\sum_g)$ is the image under μ of a degree zero divisor of the form

$$D = \sum_{i=1}^{g} (p_i - p_0)$$

on $\sum_g$.

VI. The Degenerate Fay Trisecant Identity

The one-dimensional solutions were found by exploiting a link between the Riemann Surface and the Riemann Theta Function provided by the Fay Trisecant Identity (Fay 1973). In the logic chart (Fig 4) these links are shown. There the identity is also displayed using a different notation (Sen 1988). For the sake of completeness, we write down the pinch degenerate limit of this identity based on previous work (Kalla 2012), which takes the form of a nonlinear differential equation. The NLS equations we use, can be derived from this equation.

The functions needed to express the degenerate form of the Fay Trisecant Identity are here defined. Let a, b be distinct points on $\sum_g$. Fix local parameters k_a, k_bin the neighborhood of these points. Let $\delta = (\alpha_i, \beta_i),\ i = 1,2.\cdot\cdot\ g$ be a non-singular odd characteristic. Then for any $\vec{z} = (z_1,\cdot\cdot\ z_g)$, Fay Trisecant Identity is $A = C + D + E$, where

$$A = D_a^2 \left[\ln \frac{\theta\left(\vec{z} + \int_a^b\right)}{\theta(\vec{z})} \right]$$

$$C = -\left(D_a \left[\ln \frac{\theta\left(\vec{z} + \int_a^b\right)}{\theta(\vec{z})} \right] - K_1(a,b) \right)^2$$

$$D = -2D_a^2 [\ln \theta(\vec{z})] + K_2(a,b)$$

$$E = -\Delta_a \left[\ln \frac{\theta\left(\vec{z} + \int_a^b\right)}{\theta(\vec{z})} \right]$$

where $\int_a^b = \int_a^b \vec{\omega}$ and the scalars $K_1(a,b),\ K_2(a,b)$ are given by

$$K_1(a,b) = \frac{\Delta_a \theta[\delta](0)}{2D_a \theta[\delta](0)} + D_a \ln \theta\,[\delta]\left(\int_a^b\right)$$

$$K_2(a,b) = -\Delta_a \ln \theta\left(\int_a^b\right) - D_a^2 \ln\left(\theta\left(\int_a^b\right)\theta(0)\right) - \left(D_a \ln \theta\left(\int_a^b\right) - K_1(a,b)\right)^2$$

where D_a is the operator of directional derivate along the vector $\vec{V} = (V_1, V_2 \cdot\cdot, V_g)$ while Δ_a is the operator of the directional derivate along the vector $\vec{W} = (W_1, W_2 \cdot\cdot, W_g)$ where these vectors describe the pinch distortion at a point of $\sum_g$. Thus, the identity is written down for a specific pinch deformation.

The parameters of the pinch deformation at a point *p* of $\sum_g$ are given by the vectors $(\vec{V}, \vec{W})$, as follows,

$$\omega_j(p) = \left(V_{a,j} + W_{a,j}k_a(p) + U_{a,j}\frac{k_a(p)^2}{2} + \cdots\right)dk_a(p)$$

$$D_a F(\vec{z}) = \sum_{j=1}^{g} \partial_{z_j} F(\vec{z}) V_{a,j}$$

$$\Delta_a F(\vec{z}) = \sum_{j=1}^{g} \partial_{z_j} F(\vec{z}) W_{a,j}$$

where the set of points $a_j, j = 1, 2, \cdots (g+1)$ represent pinch locations. They are special points of $\sum_g$ related to the location of the zeros of the hyperelliptic equation. The representation of the one-form

$$\omega_j(p) = \left(V_{a,j} + W_{a,j}k_a(p) + U_{a,j}\frac{k_a(p)^2}{2} + \cdots\right)dk_a(p)$$

parametrizes the signal specific deformations while the range of the label *j* captures the number of pinch points that contribute to the one-dimensional solution. Using this notation multiple component solutions of the non-linear Schrödinger (NSL) equation (Kalla 2012) can be written down. The one-dimensional limit of this solution is relevant and is explored next (Appendix VII).

VII. Soliton Limit

Soliton solutions emerge in the limit when a genus *k* surface ($\sum_k$ a subunit of $\sum_g$; *k* < *g*) degenerates into one of genus zero. The technical way of doing this has been discussed elsewhere (Kalla 2012). As a genus zero surface is conformally equivalent to a Riemann Sphere. There is a map $w(p) = w$ which maps a point p on a genus zero surface to a point w on the Riemann Sphere. In the genus zero limit we have the following result,

$$\Omega_{kk} = \ln \epsilon + O(1)$$

$$\Omega_{ik} = \ln \left[\frac{(w_i - w_k)(s_i - s_k)}{(w_i - s_k)(s_i - w_k)} \right]$$

The diagonal period matrix elements expression from

$$\Omega_{kk} = \int_{u_i}^{v_i} \Omega_{v_k - u_k} + O(\epsilon)$$

where

$$\Omega_{v_k - u_k} = \left(\frac{1}{w - w_{v_i}} - \frac{1}{w - w_{u_i}} \right)$$

and u_i, v_i are poles that appear when double points that result when the genus *k* surface degenerates to one of genus zero, are desingularized. The meromorphic differentials that then appear on the topological sphere are entirely defined by their behavior near their singularities. In this pinching limit, meromorphic functions also appear associated with the variables z_i regarded as functions of a point z of the Riemann Surface. The reason for the appearance of singularities can be understood. A pinch deformation corresponds to the shrinking of a_i loops of $\sum_k$. These loops correspond to circuits round neighboring zeros of the hyperelliptic equation that describe a genus *k* subunit

$$y^2 = \prod_{i=1}^{(2k+2)} (z - a_i)$$

that define branch points of the equation in the complex plane. Thus, a pinch deformation corresponds to two zeros coming together (a_i, a_{i+1}). When this happens the associated one-form

$$\omega_j(z) = \frac{z^j dz}{\sqrt{P(z)}}$$

become singular and so does the function

$$z_i = \int_0^z \omega_j(z)\, dz$$

since $P(z)$ now becomes

$$P(z) \to (z - a_i)^2 \prod_{j=1}^{(2k+1)} \left(z - a_j\right)$$

with $j \neq 1, i + 1$.

One technical point to note is that the expression for $\omega_i(z)dz$ written down in terms of the hyperelliptic function needs to be normalized before it can be used in the Theta Function.

The general structure of such a meromorphic function $f(w)$ is now

$$f(w) = \alpha \prod_{i=1}^{(k+1)} \frac{w - w_{a_i}}{w - w_{b_i}}$$

With a local parameter

$$k_a(w_a) = f(w) - f(w_a)$$

where we also require that

$$f\left(w_{u_k}\right) = f\left(w_{v_k}\right)$$

This requirement comes from a global constraint that the distortion parameters have to satisfy. With these variables we can explicitly identify the parameters. These parameters describe the nature of distortions and carry information about the network because they contain the location of the pinch points and deformed period matrix.

For our case $w_a = w_{a_{k+1}}, w_b = w_{a_j}$. We have

$$V_{a,k} = \frac{1}{k_a'(w_a)}\left[\frac{1}{w_a - w_b} - \frac{1}{w_a - w_{u_k}}\right]$$

$$W_{a,k} = A_{a,k} + B_{a,k}$$

$$A_{a,k} = \frac{1}{k_a'(w_a)^2}\left[-\frac{1}{\left(w_a - w_{v_k}\right)^2 + \left(\frac{1}{w_a - w_{u_k}}\right)^2}\right]$$

$$B_{a,k} = -\frac{k_a''(w_a)}{k_a'(w_a)^2} V_{a,k}$$

where $V_{a,k}, W_{a,k}$ are pinch deformation functions. Then the Theta Function becomes

$$e^{\left[\sum_{i,k=1}^{k+1}(i\pi\Omega)_{ik}\alpha_i\alpha_k + \sum_{k=1}^{k+1} 2i\pi\alpha_k z_k\right]} = det(T)$$

$$(T)_{ik} = \delta_{ik} + \frac{w_i - s_i}{w_k - s_k} e^{z_i + z_k}$$

where each characteristic $\alpha_i,\ i = 1, 2, \cdots k$ can only be 0 or $^1/_2$ and

$$z_i^j = Z_i - d_i + \beta r_{j,i}$$

$$Z_i = iV_{a_{k+1},i}x + iW_{a_{k+1},i}t$$

while

$$r_{j,k} = \ln \frac{\left[\left(w_{a_j} - w_{v_k}\right)\left(w_{a_{k+1}} - w_{u_k}\right)\right]}{\left[\left(w_{a_j} - w_{u_k}\right)\left(w_{a_{k+1}} - w_{v_k}\right)\right]}$$

and β is a constant that can take values (-1, 0, +1) while the parameters d_k are constant for the pair of points (a_j, b_j) that come together under pinch deformation.

In terms of these variables the dark soliton $\psi_j(x,t), 1 \leq j \leq k$ solution (Kalla 2012) of the non-linear Schrödinger equation can be written as,

$$\psi_j(x,t) = A_j e^{i\pi W} \frac{det(T_{j,1})}{det(T_{j,0})} e^{-i(E_j x - F_j t)}$$

where A_j, E_j, F_j are known constants (Kalla 2012). The soliton variables depend on the parameters $(w_i - s_i)$ and the variables z_i, that explicitly depend on the deformation parameters $V_{a,k}, W_{a,k}$ while the set of non-zero characteristics carry information about the network responsible for generating the signal. The deformed period matrix also appears in the solutions. The phase θ is the topological phase.

$$W = 4\sum_{i=1}^{k} \alpha_i \beta_i$$

where *W* is the topological parameter associated with spin structure and that there are *k* pulses if the system has *k* pinches. Besides these topological parameters the solution also carries the geometrical details regarding the nature of pinch deformations with them.

VIII. Soliton Solution and Data Fitting

We show that the dark N-soliton solution (Previato 1985) of the non-linear Schrödinger (NLS) differential equation, can fit recorded data of a spike train generated by a murine single thalamic neuron by means of presynaptic stimulation. The fitting demonstrates that this solution of the non-linear Schrödinger equation can represent observed action potentials that are produced in a physiological manner.

We have as the dark soliton solution:

$$\psi(x,t) = \frac{\psi_1(x,t)}{\psi_0(x,t)}$$

$$\psi_1(x,t) = \rho e^{\sqrt{-1}\theta} \sum_{\vec{n}}{}' e^{\left(\sum_{i<j} A_{ij} n_i n_j + \sum_{i=1}^{N} n_i \left(\eta_i + 2\sqrt{-1}\phi_i\right)\right)}$$

$$\psi_0(x,t) = \sum_{\vec{n}}{}'' e^{\left(\sum_{i<j} A_{ij} n_i n_j + \sum_{i=1}^{N} n_i \eta_i\right)}$$

The values of A_{ij} , α_i , β_i would be dependent on pinch deformation parameters.

$$e^{A_{ij}} = \left(\frac{C}{D}\right)^2$$

$$C = \sin\frac{1}{2}\left(\phi_i - \phi_j\right)$$

$$D = \sin\frac{1}{2}\left(\phi_i + \phi_j\right)$$

$$\eta_i = \mu_i x + \nu_i t$$

$$\mu_i = 2\rho \sin\phi_i$$

$$\nu_i = 2\rho \sin\phi_i (2\mu_0 - 2\rho\cos\phi_i)$$

$$\theta = \mu_0 x + \nu_0 t$$

$$\nu_0 = \mu_0^2 + 2\rho^2$$

$$\rho = \lim_{x\to\pm\infty} |\psi(x,t)|$$

then

$$\rho = \frac{(b_2 - b_1)}{2}$$

$$\mu_0 = -(b_1 + b_2)$$

$$\nu_0 = b_1^2 + b_2^2 + \frac{1}{2}(b_1 + b_2)^2$$

$$\sin\phi_j = \frac{2\sqrt{-1}\alpha_j\left(b_1 - a_j\right)}{(b_2 - b_1)}$$

$$\cos\phi_j = \frac{\left(2a_j - (b_1 + b_2)\right)}{(b_2 - b_1)}$$

$$e^{\sqrt{-1}\phi_j} = \frac{(a_j - 1)}{(a_j + 1)}$$

With

$$y^2 = (\lambda - \alpha_1) \dots (\lambda - \alpha_N)(\lambda - \alpha_1^*) \dots (\lambda - \alpha_N^*)$$

as the equation defining the Riemann surface, and

$$a_j = \alpha_j - \alpha_n$$

$$b_j = \alpha_j^* - \alpha_N^*$$

$$a_j^* = -(\alpha_j - \alpha_N)$$

$$b_j^* = -(\alpha_j^* - \alpha_N^*)$$

$$N = \frac{(g+1)}{2}$$

Two classes of multi-soliton solutions can be produced; bright and dark. We note again that multi-soliton trains carry with them the local surface deformations parameter values as coefficients. These deformations are theoretically different for each pulse, whether they are bright or dark solitons. Thus, the theory predicts that each pulse of a spike train will be different.

We use the solution for dark solitons as our fit. These solutions have spikes on an elevated voltage background. For the bright soliton $\psi(x,t)$ vanishes for $x \to \pm\infty$, while for the dark soliton it is a constant that reflects the background voltage, which aligns with observed results.

The sum over $\vec{n}$ is for all values of the n_i that are either $n_i = 0,1$, with $\vec{n} = (n_1, n_2, \dots, n_g)$, and $N = g$. With this the boundary condition is explicit and there are no oscillations in the x variable. The single time oscillation terms are an overall multiplicative factor. The matrix A_{ij} has been defined in terms of ϕ_i. The matrix A_{ij} is symmetric and real.

The data set here used, was obtained from a patch-clamp whole-cell recording, in current clamp mode, at 5kHz sampling rate. The recording was performed on a neuron from the thalamic posterior nucleus (Po), on a 300µm thick, acute, coronal slice of an adult mouse brain. The excitatory postsynaptic potentials (EPSPs) were evoked by means of repetitive opto stimulation with 3ms light pulses (475nm) at 20Hz, on axon terminals present in the vicinity of the recording area, that belong to corticothalamic ipsilateral projections of L5 pyramidal neurons of the primary somatosensory cortex (S1). These latter neurons had been previously labeled by a local, *in vivo* inoculation, using as a gene delivery tool AAV9.CaMKIIa.ChR2(H134R).mCherry (700nl, dilution 1:5). After 8 consecutive stimulations action potentials were elicited (extended details in methods).

We then present (Fig 5) the data of the voltage trace (red) obtained, and overlapping the fit trace (blue).

IX.A Helical magnetic trace and spin structure formation

We established (Appendix IV B) that is theoretically possible to determine the voltage profile $\psi_j(z,t)$ of the jth moving soliton pulse in a train of *N* solitons, at a point *z* of the center line of a tube of the network by solving the nonlinear Schrödinger equation. We now want to determine the surface magnetic field generated by these pulses as they move along a network tube. The first step is to replace the voltages by equivalent charge densities. This is done by using Poisson's equation (Jackson 1999) of electromagnetic theory. Thus, we replace the voltage potential by its equivalent charge distribution $\rho(z,t)$, given by,

$$\frac{d^2\psi_j(z,t)}{dz^2} = 2\rho(z,t)$$

Further simplifications are made. The expression for the charge density $\rho(z,t)$ is next written as

$$\rho(z,t) = \frac{Q(z,t)}{\Delta_j} = \frac{N_j e v_j}{\Delta_j}$$

where Δ_j is the effective width of the soliton pulse and we have written Q_j as

$$Q_j(z,t) = N_j e v_j$$

where *e* is the charge of an electron, so that $N_j e$ is the equivalent soliton charge at the point *z*. These simplifications will allow us to clearly link the way the transient magnetic field of the soliton pulses voltage produce a static helical spin magnet structure.

The transient helical surface magnetic field by a moving pulse, in the approximation described (Jackson 1999) is given by

$$B_j(z) = \frac{N_j e v}{c r_a^2}$$

where *c* is the velocity of light in the medium an r_a is the radius of the tube surrounding the moving charges. We use cgs units for our calculations. We can estimate B to be $B \approx N_j 10^{-8}$ Gauss, using $c \approx 10^9$ cm/s (Khurgin 2010), $e \approx 10^{-10}$, $r \approx 10^{-4}$, $v_j \approx 10^3$ cm/s. The last to values (r and v_j) are examples chosen to be biologically relevant by emulating axonal radius and action potential speed (Scott 2002). If the surface tube is considered to have thickness, then two such transient magnetic fields on the two surfaces, of radii $r_\pm$ will be generated with helical magnetic structures,

$$h(z, r_\pm) = B_j(z, r_\pm)\left[\cos\left(\frac{2\pi z}{r_\pm}\right), \sin\left(\frac{2\pi z}{r_\pm}\right)\right], z = v_j t$$

N multi soliton pulses will generate a sequence of transient magnetic fields

$$B(z) = \sum_{j=1} N B_j(z)$$

Static magnetic structures are created by the transient magnetic field by aligning surface spins $s_i(z),\ i = 1, 2$. These structures capture the helical nature of the transient magnetic surface field created and thus contain a magnetic trace of the parameters carried by the soliton pulses.

For a train of soliton pulses with slightly different velocities the excitation frequencies for the helical trace would be a band of frequencies. A simple representation of the transient magnetic helical curve can be written as

$$B(t) = (B\cos(\omega t), B\sin(\omega t), \omega t)$$

which then could be plotted for two values of the tube radii $r_\pm$ to emulate the theoretical thickness of the tube.

We determine the static spin structure created by the transient magnetic field of the solitons in the next section and show that they have a natural excitation frequency. The structure formed has to be preserved by the electron spin magnet interactions if it is to create a trace that can be thermodynamically stable in time.

The helical spin structure is a magnetic structure but has no macroscopic magnetic properties. This is because of a special topological property of spins, namely they reverse their orientation after a rotation of 2π. This means that neighboring spins on the helix have opposite orientations. They pair to form units that have no magnetic property and have zero spin, that naturally form coherent structures which respond to thermal disruption as a single unit. The temperature stability of this structure, with *N* spin pairs requires

$$\frac{N\mu^2}{r^3} > kT$$

where μ is Bohr magnetron, *r* the distance between a spin pair, *k* the Boltzmann constant, and *T* the temperature in Kelvins.

IX.B Spin Magnet Structure and its Frequency

We next determine the spin-magnet surface structure and its excitation frequency.

We first estimate the frequency associated with the interaction of this helical field with surface electron spin magnets by using a quantum theory formula, since the dynamical behavior of electron is governed by quantum ideas. The quantum interaction of the electron spin with an external magnetic field is given by

$$H = \mu_e \vec{B}.\vec{\sigma}$$

where $\vec{\sigma}$ are Pauli spin matrices, and $\mu_e = 2\mu$ where μ is the Bohr magneton. The Pauli matrices are operators that are used to describe the electron magnetic spin states.

Quantum theory tells us that the interaction energy H has a natural excitation frequency given by

$$\omega = \frac{H}{\bar{h}}$$

We estimate this frequency by using the previous estimate for *B* and replacing $\vec{B}.\vec{\sigma}$ by $\frac{1}{2}B$. This replacement indicates that the spin is aligned to the magnetic field. Then

$$\omega = \frac{\mu B}{\bar{h}} = \frac{10^{-19} x 10^{-8}}{10^{-27}} \approx 1$$

where we set $\mu \approx 10^{-19}$, $\bar{h} \approx 10^{-27}$ in cgs units. Thus, for a pulse carrying N_j units of electron charge, in the range $1 \leq N_j \leq 10^2$, will lead to the excitation frequencies of the static magnetic trace to be in the range $1 \leq \omega_j \leq 100$ Hz, for our estimations.

We next determine the static helical spin magnet structure. A quantum calculation is needed to do this. The time evolution of a spin is described by the operator

$$U(t) = e^{-i\frac{Ht}{\bar{h}}}$$

where

$$H = \mu\vec{B}.\vec{\sigma} = \mu\vec{\hat{n}}.\vec{\sigma}B$$

where we have written

$$\vec{B} = \vec{\hat{n}}B$$

and $\vec{\hat{n}}$ is the direction of the magnetic field $\vec{B}$. We now use the identity

$$e^{-i\left(\frac{\mu}{v_j\hbar}\right)\vec{\hat{n}}.\vec{\sigma}Bt} = \cos\left[\frac{\mu}{v_j\hbar}\vec{\hat{n}}Bt\right] - i\vec{\hat{n}}.\,\vec{\sigma}\sin\left[\frac{\mu}{v_j\hbar}\vec{\hat{n}}Bt\right]$$

The time evolution of an initial spin $S_j(0)$ in quantum mechanics is given by

$$S_j(t) = e^{-i\frac{Ht}{\hbar}}S_j(0)$$

But in our case the electrons are fixed locations along the path of the transient magnetic field and the only effect of the transient magnetic field is to align the spins at different locations it interacts with. Thus, we need to study the distributions of spins present in the helical pathway of the transient field. To do so we replace *t* by $t = \frac{z}{v_j}$, where *z* is a surface point in the pathway of the transient magnetic field. The appropriate spatial spin aligning evolution operator is $U(z)$, given by,

$$U_j(z) = e^{-i\left(\frac{\mu}{v_j}\right)\vec{B}.\vec{\sigma}z} = \cos\left[\left(\frac{\mu}{v_j\hbar}\right)Bz\right] - i\vec{\sigma}.\,\vec{\hat{n}}\sin\left[\left(\frac{\mu}{v_j\hbar}\right)Bz\right], 0 \le z \le L$$

We next write $\vec{\sigma}.\vec{\hat{n}} = \frac{1}{2}$ which is the aligned spin value projected out by the evolution operator. Thus, our static helical spin-magnet distribution $S_j(z)$ is given by,

$$S_j(z) = \left(\cos\left[\left(\frac{\mu}{v_j\hbar}\right)Bz_j\right] - i\sin\left[\left(\frac{\mu}{v_j\hbar}\right)Bz_j\right]\right)S_j(0), \qquad 0 \le z_j \le L$$

where $S_j(0)$ is the spin value at *z* = 0. It is a helical chain of electron spin magnets. The structure has no net macroscopic magnetic moment. We have already pointed out that the structure would have a natural excitation frequency. For *g* pulses there will be *g* static structures given by

$$S(z) = \sum_{j=1}^{g} S_j z_j$$

The corresponding structure will have a greater value for its magnetic strength.

FIGURES

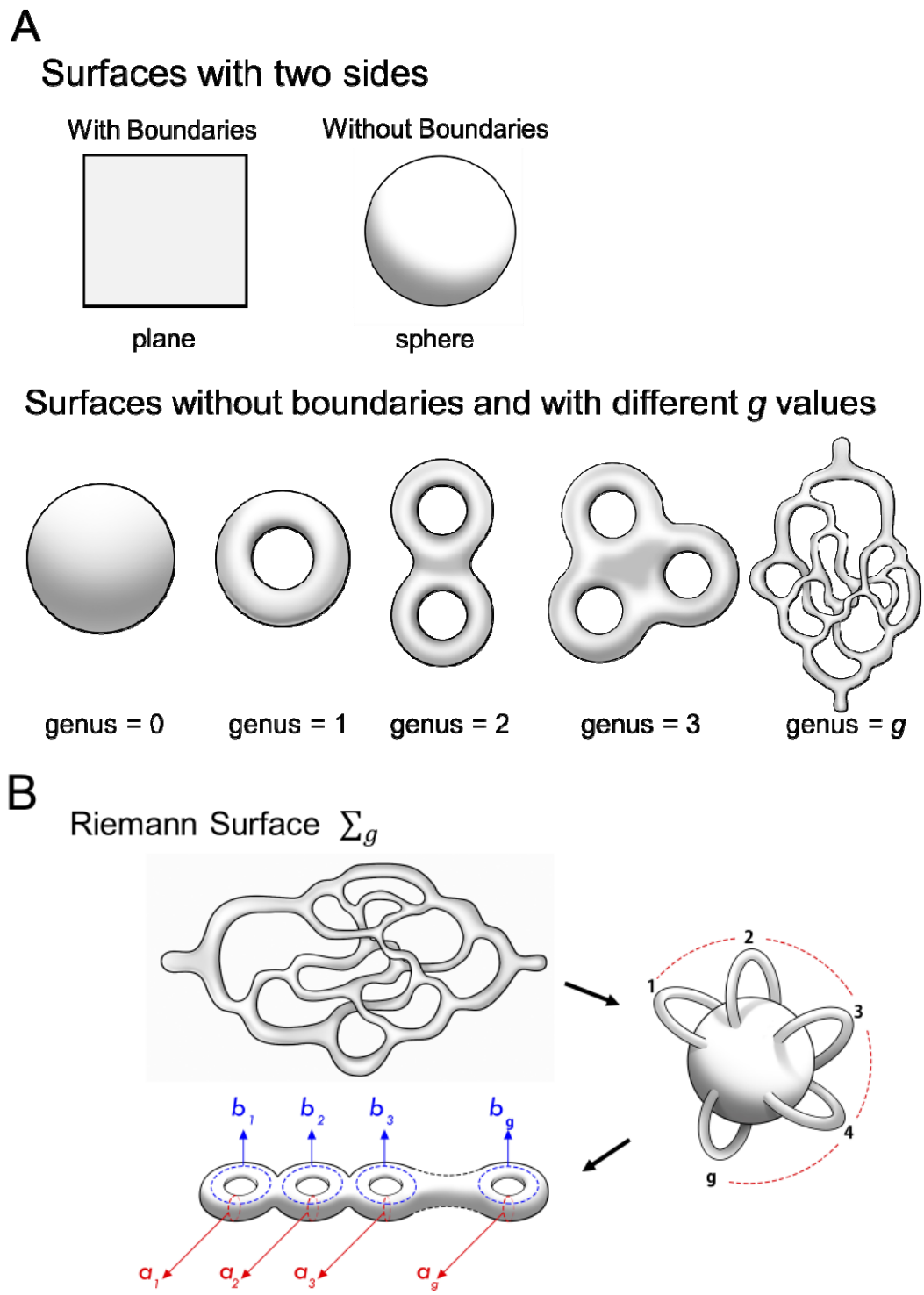

Figure 1: Topology studies surfaces in a holistic way. In this discipline, objects that can be transformed into each other are regarded as the same. **A.** A surface with two sides can have a boundary or not have a boundary. **B.** A surface without boundary, in topology, is equivalent to a sphere with g handles or an array of g donuts. The number g is the genus of the surface. All objects of genus g are the same. So that a sphere, a cube, or a tetrahedron are the same in topology (g = 0), a donut and a teacup can be regarded as the same (g = 1), but not to a teapot (g = 2) nor to a pretzel (g = 3)**.** Our surface has fixed but unknown genus g.

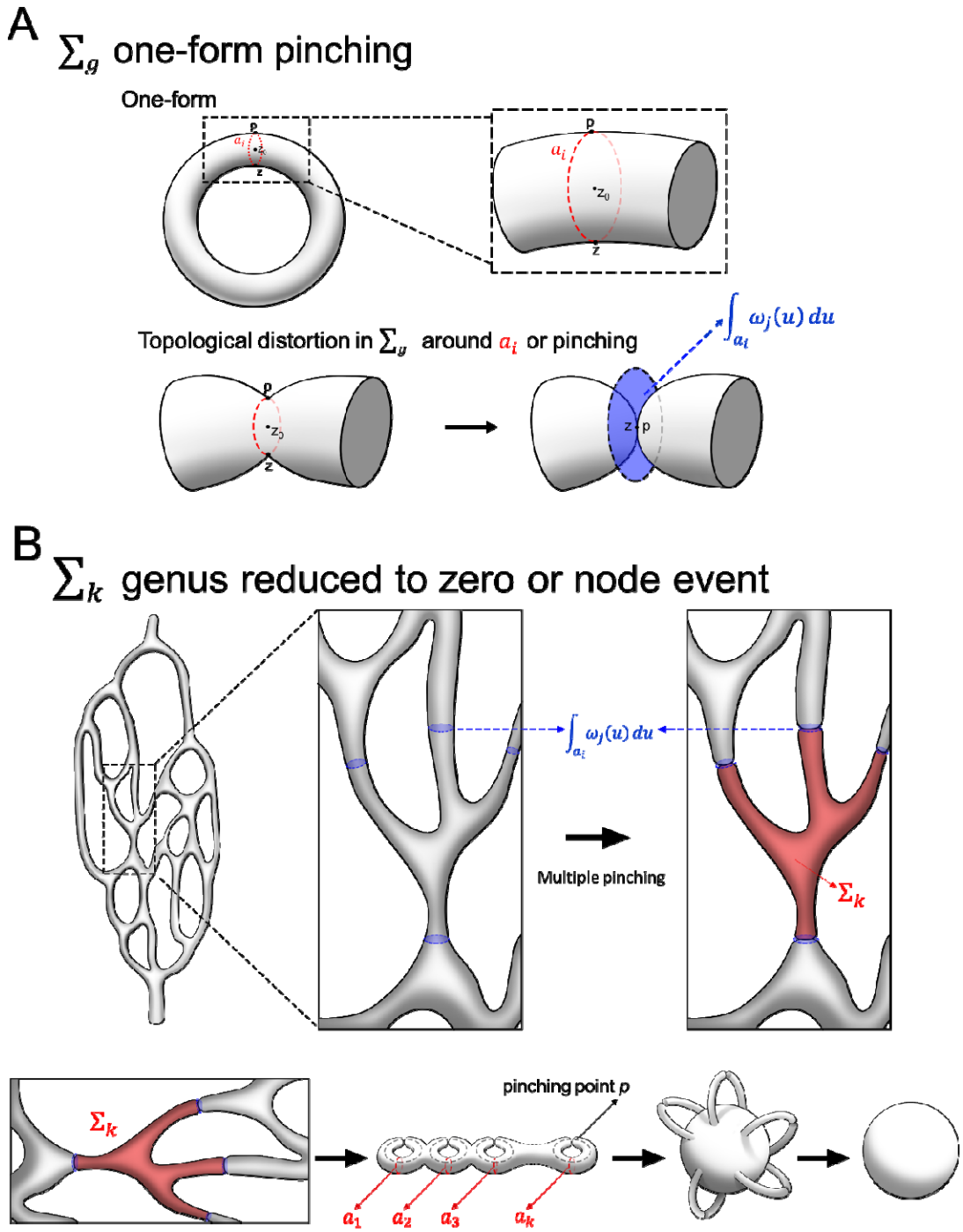

Figure 2: Local topological pinch deformations reduce, at a defined point, the circumference of a loop round a one-form to zero. **A.** The dynamic law proposed is implemented by taking the limit of the two surface-points ***p*** and ***z*** approaching each other so that an arc joining them, a sub-section of an loop connects them approaches zero. In this way the pinch deformation respects the Riemann Surface structure. This limit can be studied by considering the integral (see text for details). **B.** By pinching *k* one-forms that belong to , which is a sub-unit of the full surface-network , the subunit has its total genus value reduced to zero which transforms it transiently, into a topological sphere. We define this as a node event.

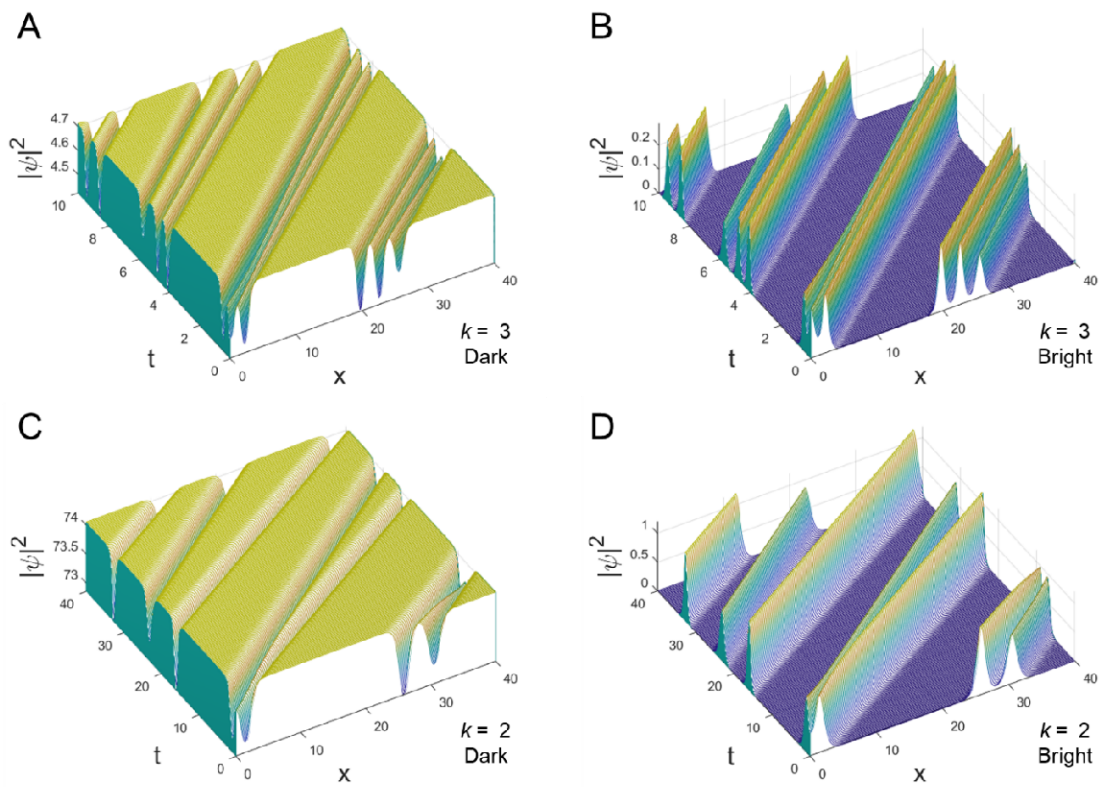

Figure 3: Numerical evaluations of multi-soliton solutions belonging to two different classes, bright and dark solitons are here plotted. The soliton solutions are evaluated as (MATLAB, MathWorks). For the parameters presented in table 1 for k = 3, **A.** One of the solutions defined as dark. **B**. The complementary solution for the same case defined as bright. For the parameters presented in table 2, for k = 2, **C.** the dark solution and the **D.** bright solution for the complementary soliton. Dark soliton solutions were obtained first. Bright soliton solutions obtained by inverting the dark solution.

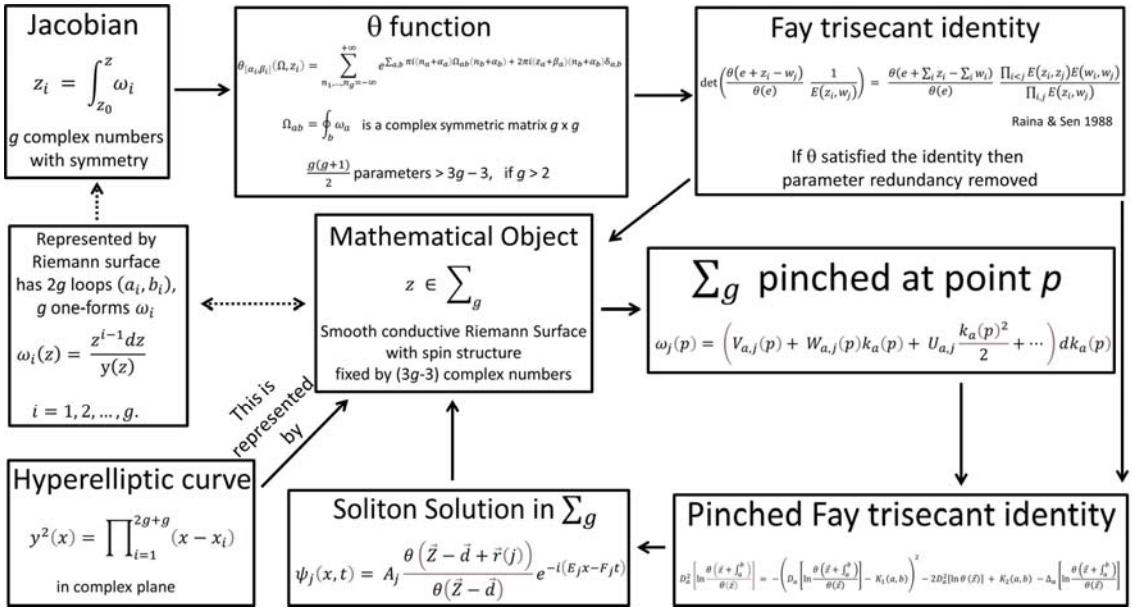

Figure 4: Mathematical diagram of the conceptual interactions that conform the presented framework, the interaction of them through the dynamical law that allows us to solve it generating soliton solutions.

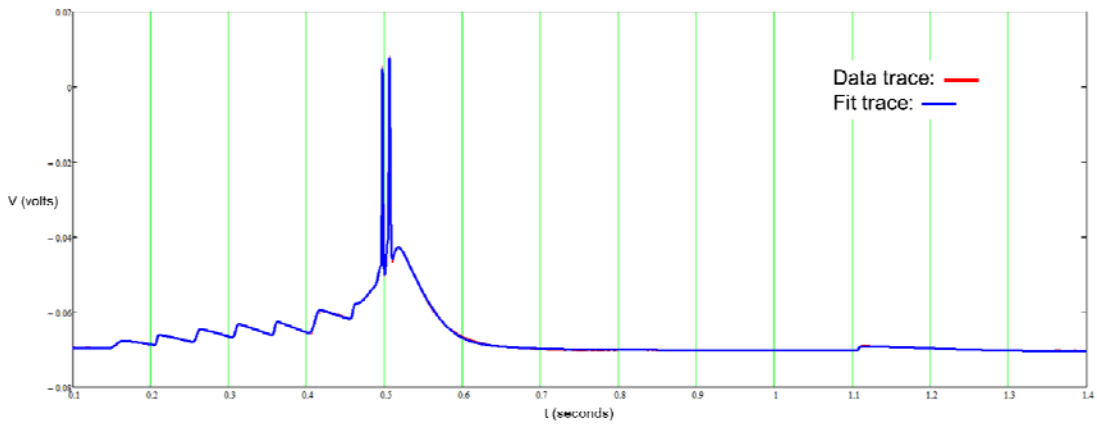

Figure 5: Recorded voltage trace (red) from an *ex-vivo* (acute slice) mouse neuron of the thalamic posterior nucleus (Po), while performing opto-stimulation to presynaptic axon terminals (ipsilateral S1 L5 pyramidal) until evoking action potentials, and overlapped the mathematical fit using the dark N-soliton solution (blue).

METHODS

Viral inoculation

Young adult (p30) male mouse C57Bl/6J wild type was placed in deep anesthesia (isoflurane) and prepared for stereotaxic cranial inoculation. The dorsal part of the animal's head, was first shaved and then disinfected topically with ethanol 70%. Under the area a subcutaneous injection, (0.1ml) of a mix of lidocaine 5mg/ml (Streuli) and Bupivacaine 1.25mg/ml (Sintetica). The mouse was placed in a dual stereotaxic frame (WPI) with drill and micropump. The animal received application of topic Carbomerum 980 2mg/ml (Bausch+Lomb) in both eyes and the body temperature was monitored and kept at 35°C (DC Temperature Controller, FHC), all through the surgery. The head skin was cleared with a vertical cut using a sterile scalpel blade. Once the area had been cleaned using sterile NaCl 0.9% serum solution (Braun), and the bleeding stopped, a small craniotomy was performed on the right parietal section of the skull to provide entry point to the inoculation. With an airtight precision syringe (10µl Hamilton, 1701 N ga26/51mm/pst3), slowly and gently moved the needle tip into the layer 5 of the right hemisphere S1 cortical area. Coordinates (Paxinos 2019) to Bregma (in mm): A.P.: -0.5 ; M.L.: +1.5 ; D.V.: -1.4. There a dose of AAV9.CaMKIIa.ChR2(H134R).mCherry (Addgene), was inoculated (700nl: dilution 1:5) at a steady rate (100nl/min). Once it was finished the syringe stayed in position for at least 10 minutes before slowly and gently retreat and exit the tissue. The animal was then sutured, received a subcutaneous dose (0.3ml) of NaCl 0.9% serum (Braun) to help hydration and was placed in a recovery cage until was ready to return to his home cage. The animal was monitored through its recovery and had Ibuprofen 20mg/ml (Verfora) in the drinking water 24h prior and 72h post the surgery. All procedures to the animal were under the supervision and authorization of DGAV-affaires vétérinaires du canton Vaud, Switzerland license VD3802, and according to EPFL veterinary regulations.

Hippocampal slice preparation

Adult (p56), male mouse C57Bl/6J wild type was placed in deep anesthesia (isoflurane) and then sacrificed. The brain was quickly extracted and placed in cold oxygenated (O_2 95%; CO_2 5%) cutting extracellular solution (in mM: 213.0 sucrose, 2.5 KCl, 10.0 $MgCl_2$, 1.25 NaH_2PO_4, 0.5 $CaCl_2$, 25.0 glucose, 25.0 $NaHCO_3$). In the same solution and with the assistance of a semiautomatic vibrating blade microtome (Leica VT1200S), acute coronal sections 300µm thick were obtained. The slices then were placed at room temperature in oxygenated (O_2 95%; CO_2 5%) normal extracellular solution (in mM: 125.0 NaCl, 2.5 KCl, 1.0 $MgCl_2$, 1.25 NaH_2PO_4, 2.0 $CaCl_2$, 25.0 glucose, 25.0 $NaHCO_3$) for at least 1h to recover before recording. All chemicals were obtained from Sigma-Aldrich.

Whole-cell patch-clamp in current clamp mode recording

The slice (coordinates (Paxinos 2019) to Bregma: A.P.: -2.30mm) was placed on a recording chamber at 33°C (Temperaturcontroller L&N) that was constantly perfused (peristaltic pump P-1, Amersham Biosciences) with oxygenated (O_2 95%; CO_2 5%) normal extracellular solution (in mM: 125.0 NaCl, 2.5 KCl, 1.0 $MgCl_2$, 1.25 NaH_2PO_4, 2.0 $CaCl_2$, 25.0 glucose, 25.0 $NaHCO_3$). Neurons were located visually using an upright microscope (Olympus BX51WI) with IR-DIC optics and a digital camera (Prime 95B Teledyne photometrics). Borosilicate capillaries with filament (Hilgenberg; 1403513) were pulled with a pipette puller (p-97, Sutter Instruments) into pipettes that were filled with intracellular solution (in mM: 110.0 K-Gluconate, 10.0 KCl, 4.0 Mg-ATP, 10.0 Na-Phosphocreatine, 0.3 Na-GTP, 10.0 HEPES, 8.0 Biocytin; pH 7.3, 295 mOsm). The intracellular electrode (Ag/AgCl) presented a resistance between 5 to 10 MΩ in the bath. Somatic, current clamp, whole cell recordings were performed using Axopatch 200B amplifiers (Axon Instrument). Data acquisition was performed via ITC-18, connected to a Windows based PC (Dell), running a custom-made routine in Igor Pro (V 9.0, Wavemetrics). The voltage signal was sample at rates between 5kHz, and filtered with a 2kHz Bessel filter. All chemicals were obtained from Sigma-Aldrich. The injected current was to obtain -70mV at steady state, previous to stimulation. The response to opto-stimulation was recorded under these conditions.

Opto-stimulation

Coupled to the microscope, a CoolLED pT-100, white light lamp controlled through digital output by a custom-made routine in Igor Pro (V 9.0, Wavemetrics), at 100% intensity, delivered light flashes

through a filter cube (Olympus U-MNBV2, 475nm), and an objective (LUMPlanFI/IR; 40x / 0.80 W; ∞/0) onto the recorded neuron and surroundings. The protocol was of 8 repetitions, duration 3ms, 20Hz, and 1 repetition 1s after first.

ACKNOWLEDGEMENTS

The authors would like to thank Mike Coey, Kumar Gupta, Mani Ramaswami and Arnab Das for encouragement, Paul Voorheis and Mike Coey for reading through an earlier version of the manuscript and making helpful editorial suggestions, Raul Ramos for his help with the figures, Tim O'Leary for useful comments, Christian Klein and Jörg Frauendiener for their kind assistance and for supplying codes used in their work on Riemann surfaces, and also to Mauro Ferreira for his guidance and support. This research did not receive any specific grant from funding agencies in the public, commercial or not-for-profit sector.

REFERENCES

- Arbarello, E.; Contemporary Mathematics 312: 9-70 (2002)
- Atiyah, M. F.; Annales Scientifique de l'École Normale Supérieure, quatrième série, 4: 47-62 (1971)
- Bak, J. and Newman, D.J.; Complex Analysis. Springer (2010)
- Barry, J., Turner, M.J., Schloss, J.M., Glenn, D.R., Song, Y., Lukin M.D., Park, H., and Walsworth, R. L.; Proceedings of the National Academy of Sciences, 113: 14133-14138 (2016)
- Belokolos, E. D.; Algebro-geometric Approach to Nonlinear Integrable Equations, Springer Series in Non-linear Dynamics. Springer-Verlag (1994)
- Bialek, W., Rieke. F., de Ruyter van Steveninck, R. R., and Warland, D.; Science 252 (5014): 1854-1857 (1991)
- Cornejo, V. H., Ofer, N., and Yuste, R.; Science 375: 82-86 (2022)
- D'Este, E., Kamin, D., Balzarotti, F., and Hell, S.W.; Proceedings of the National Academy of Sciences USA 114(2): E191-E199 (2017)
- El Hady, A. and Machta, B.; Nature Communications 6: 6697 (2015)
- Fay, J.D.; Theta functions on Riemann Surfaces, Lecture Notes in Mathematic, 352. Springer-Nature (1973)
- Feinberg, G. and Sucher, J.; Physical Review A 2: 2395 (1970)
- Guardia, J.; Journal of Algebra 253: 112-132 (2002)
- Guskjolen, A., Kenney, J.W., de la Parra, J., Yeung, B.R.A., Josselyn, S.A., and Frankland, P.W.; Current Biology 28: 2283-2290 (2018)
- Hamdan, H., Lim, B.C., Torii, T., Joshi, A. Konning, M., Smith, C., Palmer, D.J., Ng, P., Leterrier, C., Oses-Prieto, J.A., Burlingame, A.L., and Rasband, M.N.; Nature Communications 11: 100 (2020)
- Harnack, A.; Mathematische Annalen 10: 189-198 (1876)
- Jackson, J.D.; Classical Electrodynamics. John Wiley & Sons, Inc. (1999)
- Leterrier, C.; The Journal of Neuroscience 38(9): 2135-2145 (2018)
- Liu, X., Ramirez, S., Pang, P. T., Puryear, C. B., Govindarajan, A., Deisseroth, K., and Tonegawa, S.; Nature 484: 381-385 (2012)
- Kalla, C.; International Mathematics Research Notices 2013: 4170-4222 (2012)
- Kallel, S. and Sjerve, D.; Annales de la Faculté des Sciences de Toulouse Mathématiques 19: 457-477 (2010)
- Khurgin, J.; Advances in Optics and Photonics 2(3): 287-318 (2010)

- Krazer A.; Lehrbuch der Thetafunktionen. Leipzig B.G. Teubner (1903)
- Mumford, D.; Annales Scientifique de l'École Normale Supérieure, quatrième série, 4: 181-192 (1971)
- Mumford, D.; Tata Lectures on Theta II. Brikhäuser (1984)
- Munkres, J.; Topology. Pearson New International Edition. Pearson (2014)
- Nash, C. and Sen, S.; Topology and Geometry for Physicists. Elsevier Academic Press (1988)
- Ortega-de San Luis, C. and Ryan, T.J.; Journal of Biological Chemistry 298(5): 101866 (2022)
- Paxinos, G. and Franklin, K.B.J.; The Mouse Brain in Stereotaxic Coordinates 5th Ed. Elsevier Academic Press (2019)
- Previato, E.; Duke Math Journal 52(2): 329-377 (1985)
- Rasband, M.N. and Peles, E.; Cold Spring Harbor Perspectives in Biology 8(3): a020495 (2016)
- Ryan, T.J., Roy, D.S., Pignatelli, M., Arons, A., and Tonegawa, S.; Science 348: 1007-1013 (2015)
- Scott, A.; Neuroscience: A Mathematical Primer. Springer-Verlag (2002)
- Scott, H.L., Bolmatov, D., Podar, P.T., Liu, Z., Kinnun, J.J., Doughty, B., Lydic, R., Sacci, R.L., Collier, C.P., and Katsaras, J.; Proceedings of the National Academy of Sciences USA 119(5): e2212195119 (2022)
- Semon, R.; Die Mneme. Wilhelm Engelmann (1904)
- Sen, S. and Raina, A.K.; Physics Letters B 203: 256-262 (1988)
- Teleman, C.; Riemann Surfaces. Lent Lectures. Berkeley Math (2003)
- Uchida, M., Onose, Y., Matsui, Y., and Tokura, Y.; Science 311: 359-361 (2006)